On the Oxide Nanofeatures and Precipitates in the Nano-Structured Ferritic Alloy MA957: A Multiple Technique Study of Heat to Heat Variations and the Effects of Friction Stir Welding and Long Term Thermal Aging - N.J. Cunningham, A. Etienne, Y. Wu, E.M. Haney and G.R. Odette (University of California-Santa Barbara, CA).

SUMMARY

We report on work supported by the DOE Offices of Fusion Energy Sciences and Nuclear Energy on nano-structured ferritic alloys (NFAs) that contain an ultrahigh density of nm-scale Y-Ti-O nanofeatures (NFs). Our objective is to explore the characteristics (number density, size distribution, volume fraction and structure) of the NFs. Small angle neutron scattering (SANS), transmission electron microscopy (TEM), and atom probe tomography (APT) were used to characterize the NFs in MA957 in both as-extruded round bar (US heat) and thick walled tube (French heat) conditions, as well as the US MA957 following long term thermal aging (LTTA) and friction stirred welds (FSW). MA957 was found to contain ≈ 1-10x10^{23} NFs with an average diameter of ≈ 2.5 nm. The smaller NFs are cubic pyrochlore $Y_2Ti_2O_7$ oxides. The NFs coarsen slowly at 1000°C and are moderately degraded by severe deformation during friction stir welding.

INTRODUCTION AND BACKGROUND

Nano-structured ferritic alloys (NFA) have high tensile and creep strength permitting service up to more than 800°C, manifest remarkable resistance to radiation damage and can manage high concentrations of helium [1,2]. Note reference 1 contains a review of the literature up to about 2008 and will be used as the citation for a number of results in the literature described in this report. A summary of more recent work on NFA is described in [2]. NFAs typically contain 14(12-16) wt.%Cr, along with Mo or W and Y and Ti (14YWT). They are called NFAs because they contain an ultrahigh density of 1-5 nm Y-Ti-O features (NFs), which are largely responsible for their outstanding properties. The NFs provide dispersion strengthening, help stabilize dislocation and fine grain structures, reduce excess concentrations of displacement defects by enhancing vacancy-self-interstitial recombination and trap helium in fine, and relatively harmless (or, indeed, potentially beneficial) bubbles [1-4]. International Nickel Company (INCO) developed MA957 as the first commercial vendor 14Cr ODS alloy in the late 1970s for use in liquid-metal fast breeder reactors [5]. Note, however, we distinguish the 14CrYWT NFAs from ODS alloys, like higher Cr and Al INCO MA956 and Plansee PM2000, since the latter contain coarser (> 5 nm) oxide phases and are generally not as strong. Experimental ODS/NFA heats, for a range of compositions and processing routes, were studied in Japan by S. Ukai and co-workers in the 1990s, leading to the high performance Kobe J12YWT NFA. Early TEM and XRD studies indicated the presence of very fine scale oxide features in alloys such as MA957 and J12YWT [1] and 1-3 nm Y-Ti-O were first observed in APT by Kim et al. in 2000 [6].

NFA processing typically involves mechanical alloying (MA) rapidly solidified metallic powders with Y_2O_3 oxide powders by ball milling. The Y and O dissolve in the Fe-Cr-Ti matrix and subsequently precipitate with Ti during consolidation by hot extrusion or hot isostatic pressing (HIPing). NFAs are then usually further processed and fabricated into various product forms by a variety of post-consolidation thermal mechanical treatments (TMT). Ideally, the TMT result in fine grain sizes and high dislocation densities that, along with the NF, contribute to high NFA strength and, potentially, better fracture toughness.

Optimizing NFAs requires understanding of the detailed composition and structure of the NFs, as well as how alloying elements and processing variables affect their character. While it is clear that a suite of characterization tools are needed to develop such understanding, various techniques are not yet fully consistent with one another. In addition to understanding the basic NF character, other questions that are addressed in this work are NFA stability during extended service at high temperatures and finding joining methods that do not severely degrade the NFs.

MATERIALS AND METHODS

Three heats of MA957, originally manufactured by INCO, were studied [7]. The first two heats are as-extruded 1150°C, 25mm round bar that were acquired from Pacific Northwest National Laboratory are referred to as US-MA957 (DBB0114 and DBB0122). Both of these heats have been used for various research topics described in

this report and it has been assumed they are effectively similar. The third heat is a 9 mm thick, 65 mm outer diameter tube fabricated by center drilling an extruded bar followed by hot extrusion (HBB-0127). This heat was acquired from CEA Saclay in France via Oak Ridge National Laboratory and is referred to as French-MA957. The processing descriptions are nominal in both cases and the specific thermal mechanical treatment conditions are unknown. The measured compositions (at%) of the US MA957 from a previous study on the US heat [7] and current APT measurements on the French heat are shown in Table 1.

Table 1. Compositions of the MA957 Heats

at%	Fe	Cr	Ti	Mo	Y	O	Ni	Al	Mn	Si	C	Cu	S	P
DBB0114*	82.97	14.32	1.123	0.170	0.128	0.786	0.089	0.183	0.065	0.059	0.073	0.009	0.011	0.007
DBB0122*	82.19	14.97	1.206	0.177	0.125	0.781	0.093	0.142	0.067	0.049	0.171	0.009	0.012	0.009
HB-0127**	83.36	14.65	0.925	0.176	0.114	0.396	0.112	0.042	0.061	0.060	0.005	-	-	-

* Ref [7]; ** APT measurement

Long term thermal aging (LTTA) has been carried out on the US-MA957 between 800°C and 1000°C in 50°C increments for times up to more than 19kh. MA957 coupons were tightly wrapped in high Cr alloy foil, to minimize loss of this element [9], and encapsulated in quartz tubing containing dry He. Aging, which is ongoing, was interrupted periodically for microhardness measurements and nano-microstructural characterization studies. The outer region of the coupons was removed to avoid the effect of Cr depletion and other near surface effects.

The friction stir welding (FSW) was carried out by Edison Welding Institute where two 100 × 17 × 2 mm US-MA957 sectioned plates were butt-welded in the long dimension direction at a tool spindle speed of 130-160 rpm and travel speed of 150-200 mm/min [9,10]. Hardness traverses were previously carried out across the weld and coupons were removed from the middle of the FSW zone for nano-microstructural characterization [9]. In the current study the micro-nanostructure of the FSW examined by a variety of characterization methods. The characterization was also repeated on FSW after an 1150°C anneal for 3 hours, followed by air-cooling, using the same encapsulation procedure as for the LTTA samples. These annealing treatments were intended to explore the possibility of re-precipitating solutes dissolved by severe deformation during FSW.

The micro-nanostructures of the MA957 heats were characterized by SANS, APT and TEM. Nominally, APT has near atomic resolution for measuring the composition of the NFs, as well as their number densities and size distributions. However, APT samples only a very small volume of material (≈10^{-3} μm^3), which is a particular drawback for NFAs with somewhat inhomogeneous distributions of the NFs. Further, effects such as trajectory aberrations of the field emitted ions, caused by different evaporation fields for the matrix and the precipitates, can confound accurate measurements of the composition as well as the sizes and shapes of the NFs. SANS determines average size, number density, and volume fraction of NFs in bulk material, but cannot directly measure their compositions, or easily distinguish the presence of different types of NFs. However, the ratio of magnetic scattering to nuclear scattering (M/N) does contain information about the composition of the non-magnetic NFs. The combination of a number of TEM techniques can provide, perhaps, the most comprehensive characterization of the NFs, as well as the balance of NFA microstructures; however, TEM suffers several practical challenges like feature size and signal resolution limits. Thus all of these tools, as well as others not discussed in this report, are needed to develop a robust understanding of the NFs in NFAs. Here, we apply APT, SANS and selected TEM methods to the various heats and conditions of MA957. Note, the results of additional TEM studies will be reported separately.

SANS

The SANS measurements were performed at the NIST Center for Neutron Research in Bethesda, MD on the NG7 SANS instrument [11] at a neutron wavelength of λ = 0.5 nm with the two-dimensional ^{3}He detector located 1.54 m from the sample and offset by 40.65 cm to increase the q-range up to more than 3 nm^{-1}. The differential scattering cross section $d\Sigma(q)/d\Omega$ of the scattering features were derived from two-dimensional scattering measurements on 10x10x2 mm^3 MA957 coupons in a 1.7 T horizontal magnetic field. The magnetic field permits measurement of both nuclear (n) and magnetic (m) scattering, where the later depends on the angle from the horizontal magnetic field direction, θ, as.

$$d\Sigma(q)/d\Omega(\theta)_{tot} = d\Sigma(q)/d\Omega_n + \cos^2(\theta)d\Sigma(q)/d\Omega_m \quad (1)$$

The field was applied in the extrusion direction to improve the magnetization of the Fe matrix, assumed to be saturated [12,13]. Approximately 5 million detector counts were acquired for each run. The measured intensity was converted to an absolute differential scattering cross section, $d\Sigma(q)/d\Omega$, by subtracting background and empty container scattering and using the sample mass and measured transmission to normalize and calibrate the scattering intensity data to a water standard. The NF scattering was determined by subtracting the $d\Sigma(q)/d\Omega$ for a control that did not contain NFs. The control is a Fe14Cr0.9Ti0.3Mo alloy that was milled and HIP consolidated at 1150°C. Eq. 1, was used to derive $d\Sigma(q)/d\Omega_n$ and $d\Sigma(q)/d\Omega_m$ from the $d\Sigma(q)/d\Omega$ data averaged over the entire detector range of q and θ and to evaluate magnetic to nuclear scattering ratio, $d\Sigma(q)/d\Omega_m/d\Sigma(q)/d\Omega_n = M/N(q)$. The M/N were also evaluated by fitting M/N(q) averaged over a wide q-range as a function of $\cos^2(\theta)$. Plots of the log of the averaged $d\Sigma(q)/d\Omega$ data as a function of q^2 for three $\theta = 0 \pm 30°$, $45 \pm 15°$, and $80 \pm 10°$ were also used to present and examine the data.

The $d\Sigma(q)/d\Omega$ for features with a size r, volume V and number density N, is given by

$$d\Sigma(q)/d\Omega) = NV^2(\Delta\rho)^2\{3[\sin(qr) - qr\cos(qr)]/(qr)^3\}^2 \quad (2)$$

The $\{\}^2$ term is the form factor for well-separated spheres. The $\Delta\rho$ is the scattering length density difference between the matrix and NF, $\Delta\rho = \rho(mat) - \rho(nf)$. The ρ values are the known magnetic or nuclear scattering length for a specified isotope divided by the atomic volume. Since the composition and atom volume in the NFs, hence the nuclear scattering contrast, $\Delta\rho_n$, are not known, $d\Sigma(q)/d\Omega_n$ cannot be used to analyze the SANS data. However, the Y-Ti-O NFs are unlikely to be magnetic, and this assumption has been verified by measuring the temperature dependence $d\Sigma(q)/d\Omega_m$ [12,13]. Assuming the particles act as magnetic holes in a saturated Fe-Cr ferromagnetic matrix allows the $\Delta\rho_m = \rho(matrix)_m$ which is known; note, this requires properly accounting for the alloy composition [12, 13]. The distribution and average size of the NFs, N and their corresponding total volume fraction, f, were derived by least squares fitting computed scattering curves (Eq. 2) to the measured $d\Sigma(q)/d\Omega_m$ data, assuming a log-normal NF size distribution. In some cases the M/N varied significantly with q and the data assuming a single scattering feature over the entire q range did not provide a good fit to the data. In these cases the $d\Sigma(q)/d\Omega_m$ data was fit to two features with different r and M/N. Typically the second feature was very small with $r \leq 0.5$ nm with a low $M/N < 1$. It is not clear if these small features are real, or if they are artifacts of the approximate control subtraction procedure. In any case, the first larger feature is assumed to represent scattering from the actual NFs and precipitates. Further details on the data analysis is described elsewhere [12-14].

The M/N ratio also contains information on the NF composition due to their effect on the nuclear but not magnetic scattering. The composition cannot be uniquely determined from the M/N ratio, but rather the measured M/N can be compared to calculated M/N from NFs with assumed compositions such as the equilibrium bulk oxide phases $Y_2Ti_2O_7$ and Y_2TiO_5. The measured M/N, however, is to some extent affected by the approximation associated with subtracting a control that may not fully represent the scattering not associated with the NFs. Further, the assumption that the matrix is magnetically saturated may be invalid in some cases.

APT

APT was performed using an Imago Local-Electrode Atom Probe (LEAP) 3000X HR. Samples are prepared by either electropolishing or using an FEI Helios 600 focused ion beam (FIB). Electropolished samples were made from ~0.5x0.5x20 mm bars using the two stage process described by Miller [15]. FIB sample preparation used the trench method outlined by Thompson [16]. Each sharpened tip is cleaned to remove Ga damage first using a 5KeV and then a final 2 KeV beam at 28 pA. The LEAP samples were examined in voltage or laser mode for a variety of run conditions. Temperatures ranged from 33K to 60K and laser pulse energies varied from 0.05 nJ to 0.45 nJ with a green (λ = 532 nm) laser. Laser and voltage pulses were held at 200kHz repetition rate, the evaporation rate was typically between 0.5% and 1%, and in the voltage mode the pulse fraction was either 20 or 25%.

The Imago Interactive Visualization and Analysis Software (IVAS) package was used for reconstruction and analysis of the LEAP data. To improve accuracy of the reconstruction, SEM images of the needle profile (52° stage tilt) were taken at the start and, when possible, at the end of the run. The actual length of the field evaporated region was determined by superimposing ovals representing the pre- and post-run tip radii onto the SEM image and comparing the measured length with the length of the IVAS reconstructed data. If the lengths did not match, the default evaporation field (Fe = 33 V/nm) was adjusted until the IVAS reconstruction length agreed with the measured value from the SEM.

Analysis of APT data requires identifying all pertinent ion mass to charge ratios (m/c) that form a wide spectral distribution composed of specific isotopes and charge states, including ionic species, like TiO^{+2}, are also frequently field evaporated. The identity of an atom or ionic species is determined from the background-subtracted spectrum with m/c increments assigned to a particular peak in a process called ranging. The m/c spectrum is influenced by a large number of variables, such as voltage versus laser mode, specimen temperature, laser energy and even variations in the specimens themselves. Identifying the m/c peaks can be challenging because complex iron alloys have many overlapping and interfering peaks in their m/c spectrum. However, elements like Fe, Cr, and Ti have a number of isotopes, resulting in multiple peaks with some that are more isolated. The multiple peaks were exploited to better estimate the total number of ions based on the natural isotope abundance ratios using a method called de-convolution. This method allows a more accurate ion count, but ion position in the reconstruction cannot be determined separately for each ion species in a single peak. Large post-peak tails from Fe^{+2} isotopes with mass numbers from 54 to 60 are also a problem because they overlap the peaks for Y^{+3} and sometimes TiO^{+2}. The number of ions in these smaller peaks was characterized using the side-band method of systematic background subtraction of the major element tails [17]. After background subtraction the peaks are generally isolated although their corresponding ion count still has an associated uncertainty.

The NFs were identified using both isoconcentration surfaces and the maximum separation distance methods [18,19]. The total number of precipitates was counted by adding the number of complete precipitates to one-half of the precipitates on the edge of the data set [15], and was used to determine the number density as

$$N_d = \frac{N_p \zeta}{\Omega N} \tag{3}$$

Here N_p, ζ, Ω, and N are the number of precipitates, the detector efficiency (37%), the atomic volume (based on bcc iron with a lattice parameter pf 0.288 nm), and the total number of ranged ions, respectively. The size and composition of the NFs was determined using the maximum separation method for the solute ions of interest, namely Y, Ti and O, including their ionic forms like TiO^{xx} and YO^{xx}. The radius of gyration (l_g) is one method for determining the size of precipitates and is equal to the distance from the precipitate center to a radial distance containing the entire mass of the precipitate as shown in Eq. 4 [15,20]. Here, n_i is the number of atoms at, r_i, which is the atom's distance from the center of mass, and n is the total number of atoms in the cluster. This so-called radius of gyration is related to the actual physical radius of the cluster r, as $r = 1.29 l_g$ [15,20].

$$l_g = \Sigma n_i r_i / n \tag{4}$$

Consistent with other studies [21, 22], the clusters were found to nominally contain significant quantities of Fe and Cr. This is believed to be an APT artifact associated with trajectory aberrations caused by different evaporation fields between the matrix and the clusters [21, 22]. If, as is the case for the NFs, the species in the cluster have lower evaporation fields, they are emitted preferentially and earlier than the matrix ions. This causes a dimple shaped local topology change in the needle tip, that images as a dark region in field ion microscopy micrographs. In this case, the cluster species and adjoining matrix ion trajectories overlap (are mixed with) one-another. An increase atom density in the cluster signals this condition. In contrast to the actual sequence of ion emissions, the reconstruction algorithm assumes the atoms are uniformly emitted from the tip of the needle one layer at a time in the z-direction. The consequences of this approximation are further discussed below with a specific example.

However, as a practical matter, the excess Fe should be removed in establishing the cluster compositions. If other information suggests that the cluster is unlikely to contain any significant quantity of Fe, then a practical expedient

is to simply remove it in estimating the cluster composition, using only the solute content. High concentrations of matrix solutes, like Cr, are also artificially enriched in the clusters. Examples of other APT artifacts, include the possibility of pre-emission of some species that are then not detected, surface diffusion, perhaps stimulated by the high electric fields and the presence of low index poles, fine scale structures like precipitate-matrix interfaces, surface ledges and ledge kinks, uneven temperature distributions during the laser pulse and several others. Indeed, given the local variations in the binding energies of various atoms in a cluster, the overall emission process inherently involves a wide range of evaporation potentials. In the present case, a variety of these aberrations appear to be operative. The Y is concentrated in the center of the clusters while the Ti and especially the O atoms are nominally more diffuse. A corrected composition can be found by completely removing the Fe and other matrix elements (e.g., Cr) based on the ratios of the solute to Fe in the matrix [21,22,23]. It is not necessary to carry out decomposition and deconvolution on the m/c spectrum of clusters removed from the matrix, since the overlapping peaks and post peak tails of the major elements in the cluster m/c spectrum are greatly reduced.

TEM

The nanoscale features were observed in both thin TEM foils and on extraction replicas. Precipitates were extracted from the NFAs by etching the surface, applying a 10-20 nm carbon coating, and then electrochemically removing a deposited carbon film with a solution of 1% tetra methyl ammonium chloride-10% acetyl acetone-methanol. Thin TEM foils were prepared in an FEI-Helios-FIB using the in situ lift-out technique. The final thickness of the thin foil is between 30 and 70 nm. A final, low energy Ga beam (2kVand 5.5pA) cleaning step was used to remove the high-energy ion damage to achieve high quality samples. Scanning transmission electron microscopy (STEM) high angle annular dark field imaging (HAADF) studies were performed using an FEI TITAN at 300 kV. Conventional bright field scattering contrast (diffraction contrast) TEM imaging and high-resolution transmission electron microscopy (HRTEM) imaging (phase contrast) studies were performed on either an FEI TITAN at 300 kV or an FEI T20 TEM/EDX at 200 kV. EDX spectra were recorded in STEM mode with the stage tilted to alpha=10˚, at a spot size of 3 or 4, and condenser aperture of 70 µm, which is the optimal experimental condition for taking EDX data from such small features. The analysis of the HRTEM images was carried out by fast Fourier transformation (FFT). The lattice spacing and inter-planar angles were measured by using Image J and Adobe Photoshop 6.0.

RESULTS AND DISCUSSION

Characterizing the NFs and precipitates in MA957

SANS

SANS measurements were performed on the US MA957 during four separate NIST campaigns and two campaigns in the case of the French heat. Figure 1a shows example absolute q = 45±15 averaged $d\Sigma(q)/d\Omega$ curves. The 45±15 curve has the largest q range and includes contributions from the nuclear plus ≈ 50% of the magnetic scattering. Both heats show an almost identical bulge in scattering compared to the control. Figure 1b shows an example NF $d\Sigma(q,q)/d\Omega$ curves, derived by subtraction of the control from the NFA scattering, plotted as a function of q^2. The solid lines are two-feature least square fits to the q averaged data at 0 ± 30°, 45 ± 15° and 80 ± 10°.

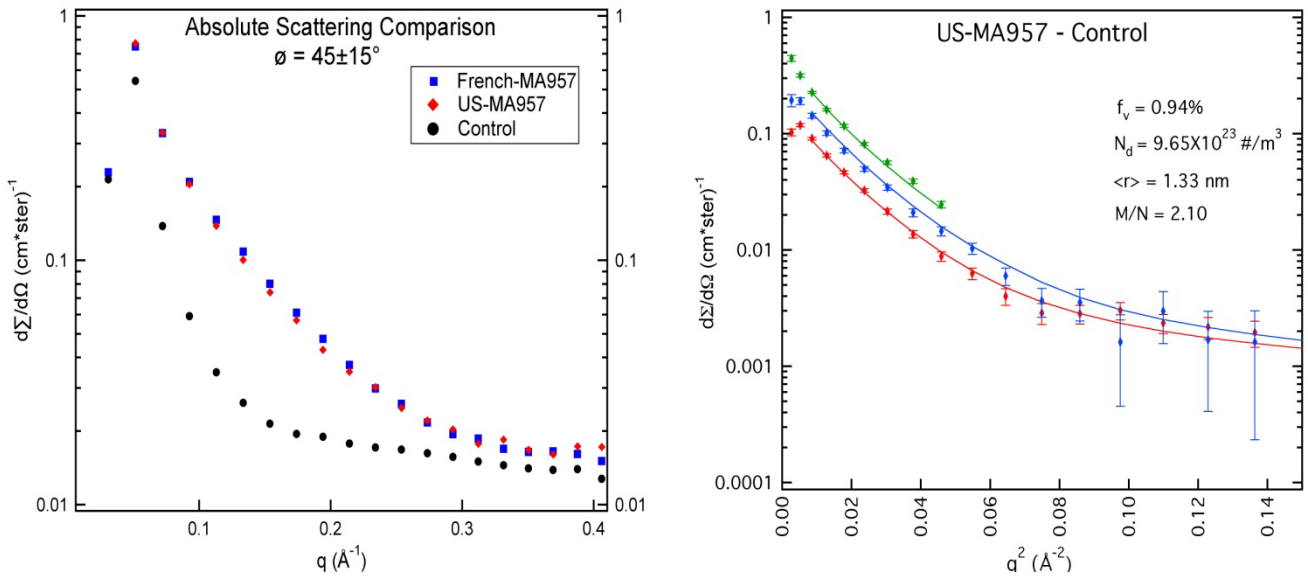

a. b.

Figure 1. a) Comparison of US-MA957, French-MA957, and control scattering 45° curves; b) example fits to scattering data for NFs in the US-MA957.

The average r, N, f, and M/N for the US and French MA957, and the corresponding one standard deviation errors, are shown in Table 2. The precipitate size is essentially identical in both heats, while the N and f are nominally slightly smaller in the French-MA957. There is a larger difference in the M/N ratio, ranging from ≈ 1 (French heat) to 1.9 (US heat). As noted previously, there are a number of reasons that explain the range of measured M/N. First, the measured M/N depend on the magnetization of the matrix that may not have been fully saturated in all cases, leading to lower M/N. Further, the method for isolating the NF scattering by subtracting the scattering from a nominal control is approximate and may lead to some differences in the measured M/N. Of course, the variations in the M/N may also reflect real differences in the NFs and precipitates in the two heats of MA957. The M/N can be calculated for assumed NF compositions and structures of $Y_2Ti_2O_7$ and Y_2TiO_5; the M/N are both ≈ 1.4 in both cases. This suggests that the NFs in MA957 are not stoichiometric bulk oxides. Higher Ti and lower atom densities lead to smaller M/N, while lower Ti and higher atom densities increase M/N. Any Cr and Fe that is artificially included in small NF due to SANS resolution limits, or as actual constituents of the Y-Ti-O or other fine scale scattering features, also increase M/N. Further, it has been shown that differences in alloy compositions and processing conditions have a significant effect on the M/N [13], so heat-to-heat variations are not unexpected. Given the uncertainties in measuring and interpreting M/N, the SANS data are broadly consistent with somewhat non-stoichiometric oxide compositions and atom densities.

Table 2. SANS N,<r> and f for the US and French MA957

Alloy	N (#/m^3)	r	f_v	M/N
US-MA957	9.40±0.93X10^{23}	1.33±0.01	0.93±0.08	1.92±0.14
French-MA957	7.56±1.00X10^{23}	1.32±0.03	0.72±0.04	1.13±0.12

APT

APT measurements were carried out on one French and nine US MA957 samples. Small Y-Ti-O enriched NFs were observed in all cases and larger precipitates were found in some of the reconstructions. Figure 2a shows a region containing a relatively uniform distribution of small NFs. Figures 2b and c show front and side views of a sample containing a mixture of small NFs and larger precipitates in the US MA957. The large precipitates appear

to be aligned, most likely on a grain boundary lying just outside the data set. The single French MA957 sample had a very high density of small, uniformly distributed NFs.

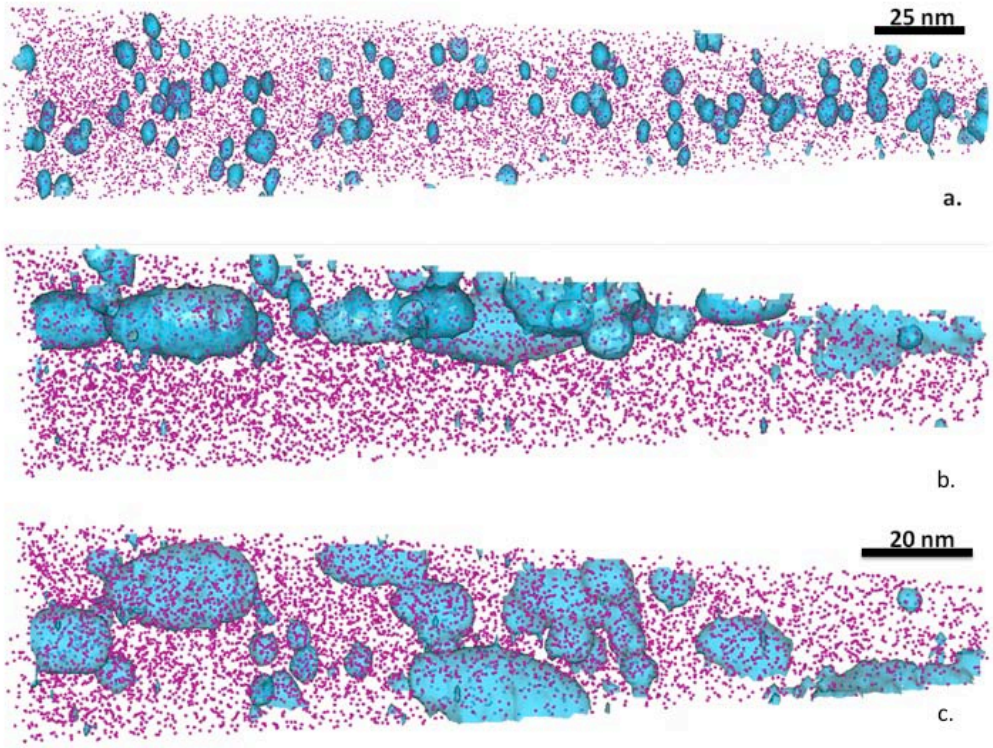

Figure 2. Isoconcentration surfaces showing: a) A US MA957 needle with a uniform distribution of small NFs; b) front and c) side views of a needle with large precipitates on the edge of the data set, possibly on a boundary.

APT run conditions such as temperature, laser or voltage mode, laser power, sample orientation, etc. can affect the m/c resolution. The APT compositions for the US MA957 in Table 3 are for a m/c spectrum with high resolution that was analyzed using the peak decomposition and de-convolution methods described above. The first two columns in Table 3 compare the previously measured bulk composition to that measured in the volume shown in Figure 2b and c. The agreement is generally good except for the Y. This difference is probably due to the fact that the small volume sampled contains a locally high volume fraction of the large precipitates. Table 3 also shows the matrix composition of the APT dataset shown in Figure 2 after removing the precipitates. The matrix analysis shows that the Y, O and Ti are highly depleted relative to their bulk values, consistent with the fact that these elements are associated with the NF and larger precipitates.

The NFs and precipitates were separated into large (r>2.5 nm) and small (r<2.5 nm) size categories for composition measurements. Note the larger precipitates often fall on the edge of the reconstruction volume, hence cannot be completely analyzed. The compositions of the small NFs and a larger precipitate in the US-MA957 shown in Figure 2a are shown in Table 4. Note, as previously discussed, the nominal Fe and Cr contents are high due to trajectory aberrations. Corrected compositions are also shown in Table 4. The average Y/Ti/O ratio of the small NFs in both US and French-MA957 are similar at ≈ 14/44/42 and 13/48/40, respectively. The average Y/Ti/O ratio for the larger precipitates is ≈ 18/34/48 for the US-MA957. Note the Y/Ti and O/(Y+Ti) are much lower than for the equilibrium oxide phases in the Y-Ti-O system: Y_2TiO_5 (25/12.5/62.5) and $Y_2Ti_2O_7$ (18/18/64). However, these results are consistent with other atom probe data [1,2].

Table 3. Bulk chemistry and APT total and matrix compositions of US MA957

At%	Nominal	APT US-MA957	APT US MA957 Matrix
Fe	82.97	82.49	84.06
Cr	14.32	14.51	14.71
Ti	**1.123**	**1.181**	**0.648**
Mo	0.170	0.118	0.120
Y	**0.128**	**0.318**	**0.006**
O	**0.786**	**0.929**	**0.075**
Ni	0.089	0.113	0.116
Al	0.183	0.095	0.012
Mn	0.065	0.078	0.079
Si	0.059	0.070	0.032
C	0.073	0.006	0.006
Cu	0.009	-	0.014
B	-	0.003	0.002
Co	-	0.043	0.052
V	-	0.044	0.045
Nb	-	0.004	-

Table 4. Composition of small NFs in the MA 957 including a matrix corrected composition.

Element at%	Fe	Cr	Mo	Ti	Y	O	Al	Mn	Si	B	C	Co	V
Small NF	73.82	12.71	0.133	5.536	1.550	5.713	0.133	0.089	0.044	-	0.044	-	0.089
Corrected	-	-	0.215	38.86	12.09	46.77	0.957	0.150	-	-	0.312	-	0.377
Larger Precipitate	72.67	13.73	0.141	5.48	1.45	5.71	0.216	0.075	0.083	0.125	0.008	0.125	0.033
Corrected	-	6.70	0.248	32.59	9.53	47.63	1.36	0.043	0.149	0.814	-	0.590	-

Figure 3 illustrates another artifact that can occur in APT measurements, in this case for a large precipitate. The specific run conditions were: 30K, 200kHz pulse rate, 0.5% evaporation rate, and 0.3nJ laser pulse energy. The nominal precipitate length is more than 20 nm. The elongated shape of the feature and the distinct TiO tail on the bottom are APT artifacts. The precipitate ions have a lower evaporation field, thus are evaporated more rapidly and earlier than the matrix atoms, creating a dimple in the needle surface. The resulting local convex-concave radii resulting in the matrix-feature mixing effect and some spreading in the x-y direction as noted above. The elongation artifact arises from the IVAS algorithm that assumes all the ions are uniformly removed, layer-by-layer, over a hemispherical tip shape, when in fact the Y, Ti and O ions are actually emitted earlier in the sequence, and at a higher z-position. As a result the position of the Y, Ti and O ions are artificially extended in the z-direction in the reconstruction. The TiO tail represents another artifact, since it always appears on the bottom of the precipitates, which in fact do not have a top and bottom. This behavior has been previously observed and may be indicative of a core/shell structure [22], although the exact mechanism is not understood. One possible explanation is that the TiO ions in a shell region have a higher required evaporation field than the core of the precipitate. If the core has the lowest evaporation field these ions are removed (scooped out) first leaving a pocket still surrounded by the shell on the needle tip surface. After the core has been removed, the shell would continue to evaporate at a slower rate. However, the reconstruction algorithm would incorrectly assign the shell ions to a deeper z-position at the bottom of the precipitate. Other atom positioning artifacts of APT are surface

diffusion, perhaps stimulated by high electric fields, and preferential-delocalizing effects of the plane-pole crystallography of the needle tip.

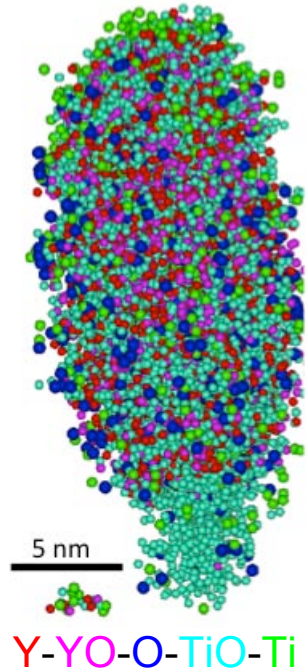

Figure 3. a) Large elongated precipitate in US-MA957.

The APT measurements give an average number density N≈ 1.8x10 ^{23}/m^3 and average diameter <d>≈ 2.3 for the US MA957, versus N≈ 6.0x10 ^{23}/m^3 and <d>≈ 3.1 for the French heat. Note significantly higher N have been previously found in other studies of US MA957, including some of our own results. The N and <d> of the NFs measured in SANS, APT and TEM are shown in Table 5, including data that will be reported separately [Y. Wu et. al. to be published]. The <d> are in good agreement for the various techniques in both heats of MA957. However the number densities vary over factors of≈ 3.5 to 5.5 between the various techniques and factors of ≈ 1.25 to 3.3 for the two heats. These differences are likely to be partly due to the inhomogeneity in the NF distributions. The overall technique averages are similar for the two heats: US heat <d> = 2.5 nm and N = 5.6x0^{23}/m^3; French heat <d> = 2.7 nm and N = 5.3 x0^{23}/m^3.

TEM

Further composition comparisons, including TEM results, will be reported elsewhere. However, in summary, the TEM results show:

Excluding TiO_x and other coarser carbon/nitride phases, HTREM-FFT measurements of plane spacing's and inter-planar angles show that the diffracting features in the size range from 8-20 nm are primarily consistent with variants of orthorhombic Y_2TiO_5, and in a few cases $Y_2Ti_2O_7$, as well as unidentified phases. EDX shows Y/Ti ratios generally between 1 and 2, and the individual oxides are non-stoichiometric.

The HRTEM-FFT diffraction measurements of plane spacing's and inter-planar angles, as well as electron powder diffraction, suggest that the smaller < 8 nm NFs are most consistent with cubic $Y_2Ti_2O_7$ with near stoichiometric Y/Ti ratios ≈ 1 and with nominal O/(Ti +Y) ≈ 2.1.

The compositions and oxide structures measured by TEM are not consistent with the APT composition values.

These results represent a significant advance in the understanding of smallest NFs. Additional research is being carried out to establish the small NF (e.g., $Y_2Ti_2O_7$) orientation relationships with the ferrite matrix. The fact that the NFs now appear to be near to equilibrium phases, rather than far from equilibrium solute clusters as previously believed based on APT data interpretations, is very important since it opens new opportunities for both experiment and modeling.

Table 5. Number density and average diameter of NFs in MA957

NF parameters	Technique	US-MA957	French-MA957
Average diameter (<d> nm)	TEM	2.5	2.6
	APT	2.3	3.1
	SANS	2.7	2.6
Number density (N 10^{23} m^{-3})	TEM	5.6	2.2
	APT	1.8	6.0
	SANS	9.4	7.6

Friction Stirred Weld Study

The US heat of MA957 joined by friction stir welding (FSW) was previously examined by TEM and SANS [9]. The severe deformation in the joint region of the FSW produced a uniform, fine-scale (≈ 0.7 μm) equiaxed ferrite grain structure, with a high dislocation density. This contrasts with the baseline MA957 microstructure with grains elongated in the extrusion direction, with aspect ratios of ≈ 5/1. The FSW process also appeared to slightly coarsen the NFs, decreasing N by an average factor of ≈ 0.5±0.1 and increasing d by about a factor of ≈ 1.2±0.08. Microhardness and tensile measurements showed a modest reduction of ≈ 7.5±1.5% in the strength of the joint compared to the as-extruded MA957. In the present work the microstructures of the FSW are re-examined using more advanced TEM and newly applied APT techniques. The FSW was also studied in the 1150°C/3h annealed state to determine if any significant degree of thermal recovery of the NFs is possible.

Figure 4 shows the FSW grain microstructure before and after annealing. Figure 4a shows the microstructure in the as-FSW condition consists of a uniform distribution of fine-scale equiaxed grains containing a high number density of dislocations. Figure 4b shows that the 1150°C/3h anneal does not have any discernable effect on the MA957 FSW microstructure at this length scale.

The TEM at higher magnification in Figure 5 shows a high number density of NFs, in the as FSW. Figure 6 shows the NFs after annealing. The N ≈ 5.6x10 $^{23}/m^3$ in the as-extruded condition versus 1.1x$10^{23}/m^3$ in both the FSW and FSW plus annealed conditions. The corresponding <d> are 2.5 and 2.9 nm, respectively. Note these are not one-to-one comparisons since the as-extruded data is based on the average of a number of studies, while the FSW cases are for more recent and limited measurements. However, TEM suggests that FSW significantly decreases N and slightly increases d. The faceted interfaces of the features, especially in Figure 6b, are particularly notable and consistent with oxide NFs down to the smallest sizes. The features are also aligned along grain boundaries and/or dislocations.

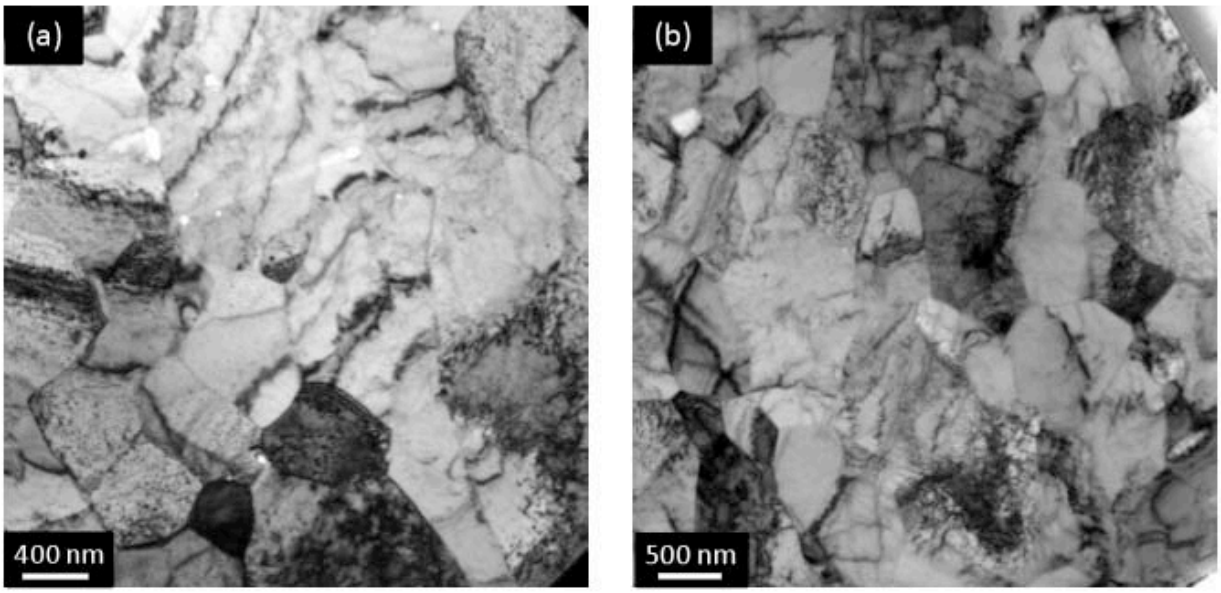

Figure 4. TEM images of the grain and dislocation microstructure in the MA957FSW (a) before and (b) after annealing 3h at 1150 °C.

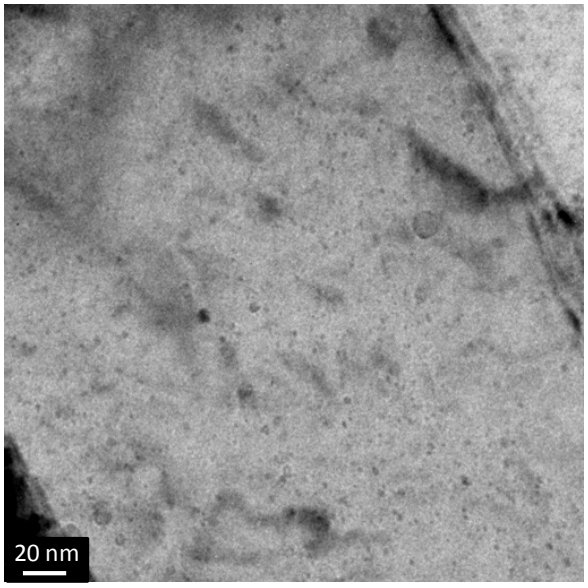

Figure 5. TEM images of NFs in the MA957 FSW.

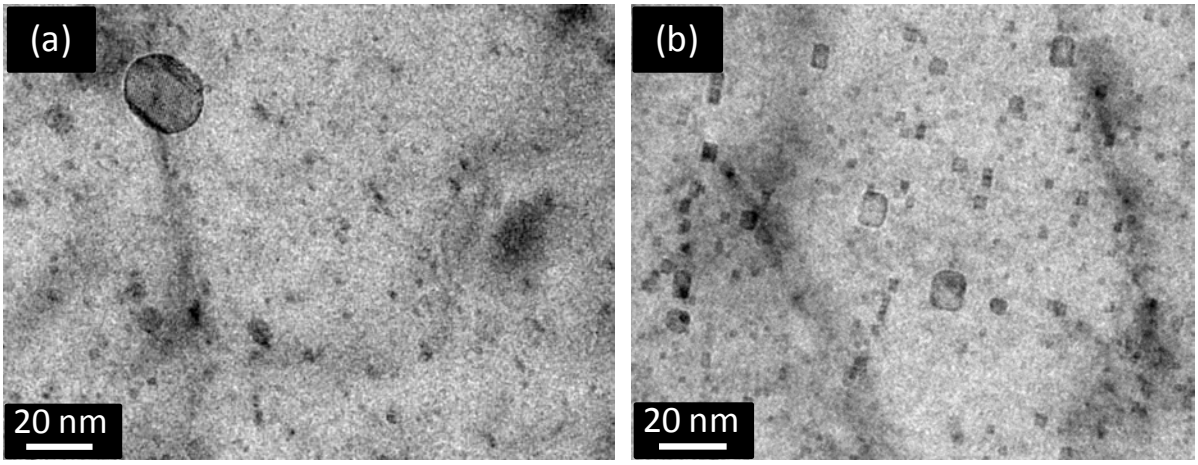

Figure 6. TEM images of the NFs in the FSW and annealed MA957.

The APT reconstruction in Figure 7 shows a fine distribution of NFs that appear to be far more aligned with grain boundaries and dislocations than in the as-extruded MA957. However, the compositions of the NFs are similar in both cases. Figure 7 also clearly shows that the distributions of O and TiO are much broader than for the Y and YO species. Such possible core shell structures have been reported in several studies of steels with small Y-Cr-O and Y-Ti-O features characterized by APT [22]. However, this also may be an APT artifact due to chemically dependent shifts in nominal versus actual atom positions which has been referred to as APT chromatic aberrations [22,23], as well as the trajectory aberrations and the artifacts due to evaporation field differences that result in a species dependent evaporation sequence, as discussed previously. In this case the YO and Y atoms are evaporated before other species.

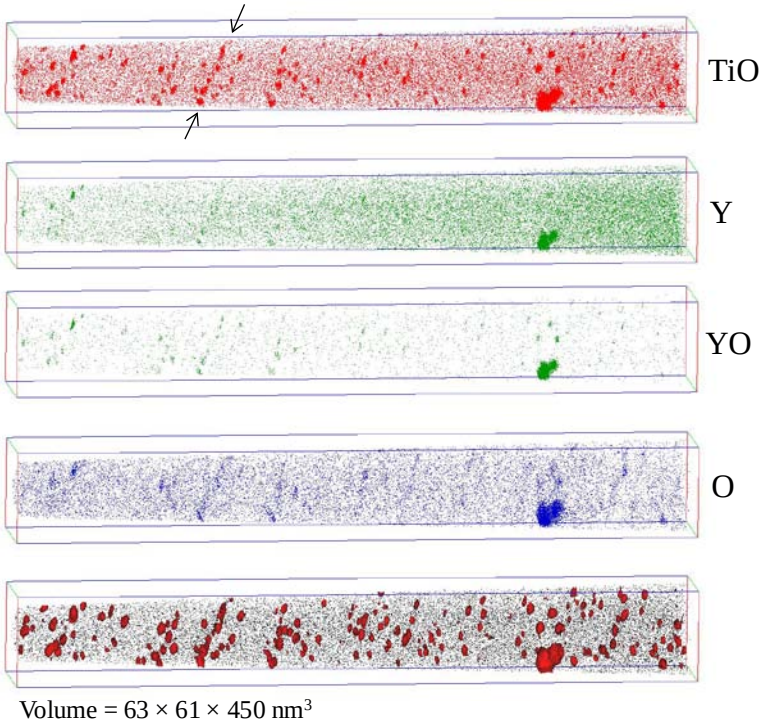

Figure 7. 3-D reconstruction of a MA957 FSW analyzed by APT. Separate TiO, YO, Y and O map atoms are shown in the top 3 reconstructions. The Ti atoms are shown in black and NF in red isoconcentration surfaces in the bottom reconstruction.

The radius and composition of the NFs in the FSW were determined using a maximum separation distance of 0.8-0.9 nm and erosion distance of 0.4-0.45 nm for the TiO, YO and Y ions. The d ranges from 1.3 to 3.6 nm, although a few larger than 5 nm were observed. The <d> 2.2 nm and the average N ≈ 1.7 ± 0.2 × $10^{23}/m^3$. These are only slightly smaller than the corresponding NF <d> and N in the as-extruded MA957, thus the APT data suggest that FSW has a minimal to modest effect on the NF. Table 6 summarizes the APT and TEM results along with previous SANS measurements [9]. Overall FSW has a minimal effect on <d> and results in decreases in N by factors ranging from 1.05 to 5.5, and averaging 2.7. Annealing has no discernable effect on the NFs. However, since there was only one APT measurement on this condition to date, the corresponding <d> and N remain to be determined.

Table 6. Comparisons of N and <d> of the NFs in FSW MA957

NF Parameter	Technique	US-MA957	FSW	FSW + anneal
<d> nm	TEM	2.5	2.9	3.0
	APT	2.3	2.2	TBD
	SANS	2.7	2.5	-
N 10^{23} m^{-3}	TEM	5.6	1.1	1.1
	APT	1.8	1.7	TBD
	SANS	9.4	3.5	-

Small oxide particles are enriched in Ti, Y, O and Al, and their composition in the FSW sample is given in Table 7. Both measured and matrix-corrected [21] compositions are shown in Table 7. The Y/Ti/O ratios are ≈ 15/40/45 and the Y/Ti≈ 0.38, that again do not correspond to known stoichiometric oxides. APT also found some larger features with N ≈ 3±2×$10^{21}/m^3$ and <d> ≈ 6 nm. These features are sometimes found to be associated with one another. The larger features are generally enriched in Ti, Y, O and Al. The Y/Ti/O ratio of the large features is 21/29/50 and the Y/Ti ratio is 0.7, which is closer to the composition of $Y_2Ti_2O_7$.

Table 7. Composition of small NFs in the MA957 FSW.

Element at.%	Fe	Cr	Mo	Ti	Y	O	Al	Mn	Si	B	C	Co	V	P
Nominal	67.8	13.8	0.20	6.5	2.2	6.7	0.28	0.10	0.13	0.11	0.04	0.10	0.06	0.03
Corrected	-	10.4	0.39	34.4	12.7	38.5	1.4	0.56	0.43	0.61	0.17	-	0.15	0.13

Long-term Thermal Aging (LTTA) Study

Long-term thermal aging (LTTA) studies are being carried out on US-MA957 from 800 to 1000°C in 50°C increments. We report here on SANS studies of the NFs after LTTA at 950 and 1000°C for times between 3kh and 19kh and TEM and APT characterization for the 1000°C, 19kh aging condition. The SANS results are shown in Figure 8. Significant coarsening is observed at 1000°C, as characterized by a decrease in N from 9.4 to 2.3x10^{23} /m^3 (Fig 8a) an increase in <d> from 2.7 to 3.9 nm (Fig. 8b) and a slight decrease in the NF volume fraction f (Fig. 8c) and microhardness (Fig. 8d). TEM measurements show decreases in N from 5.6 to 1.6x$10^{23}/m^3$ and increases in <d> from 2.5 to 2.3 nm

APT measurements also show that the NFs coarsen somewhat with decreases in N from 1.8 to 0.67x$10^{23}/m^3$ and increases in <d> from 2.3 to 2.6 nm. Finally TEM indicates such coarsening with decreases in N from 5.6 to 1.6x$10^{23}/m^3$ and increases in <d> from 2.5 to 3.0 nm. These results are summarized in Table 8. On average N decreases by a factor of≈ 3.4±0.7 and <d> increases by a factor of ≈ 1.33±0.15. Figure 9 compares the size distribution of the as-extruded and LTTA MA957 measured by APT and TEM, again showing a slight amount of coarsening.

One significant effect of the LTTA was a large reduction in the total Ti content of the MA957 from nominal levels of ≈ 1.1 to 0.22 at.%. Most of the Ti was found to be associated with the precipitates while the balance was missing from the matrix. However, the composition of the NFs is only modestly affected, with a slight decrease in Ti level. The average Y/Ti/O ratio for the small precipitates was 15.7/37.0/47.3, which is still highly non-stoichiometric. This effect is under further investigation.

Table 8. Comparison of N and <d> of NFs in as-extruded and LTTA MA957

NF N or <d>	Technique	US-MA957	LTTA
Average diameter (<d> nm)	TEM	2.5	3
	APT	2.3	2.6
	SANS	2.7	3.9
Number density (N 10^{23} m^{-3})	TEM	5.6	1.6
	APT	1.8	0.67
	SANS	9.4	2.3

CONCLUSIONS

The multi-technique analysis the NFs and precipitate oxide phases US MA957 in various conditions and a French-MA957 heat yielded the following conclusions.

SANS, TEM and APT characterization of MA957 show N, <r> and F are in reasonable to good agreement for the various techniques, with 1-10x10^{23}/m^3, <d> ≈ 2-3 nm NFs, along with a lower density of various larger oxide precipitates.

The nominal APT measurements indicate that the NFs contain a large amount of Fe. This is believed to be an APT artifact, largely associated with trajectory field evaporated ion aberrations.

The compositions of the NF in APT measurements are deficient in Y and to a lesser extent O compared to stoichiometric $Y_2Ti_2O_7$ and Y_2TiO_5 phases.

The Y and O deficiencies may be due to either a core shell NF structures, or APT artifacts, or a combination of both.

TEM indicates that the larger (> 8 nm) NFs are primarily non-stoichiometric Y_2TiO_5 or oxide phases that cannot be identified with Y/Ti ≈ 1 to 2.

TEM indicates that the smaller (< 8 nm) NFs are approximately stoichiometric $Y_2Ti_2O_7$ oxide phases with Y/Ti ≈ 1.

The NFN decrease in FSW and FSW plus annealing conditions compared to the as extruded condition, accompanied by a slight increase in <d>.

The overall effect of FSW on the strength of MA957 is modest.

The NFs slowly coarsen for long term thermal aging at 1000°C for more than 19kh.

The effects of thermal aging on the strength of MA957 are modest.

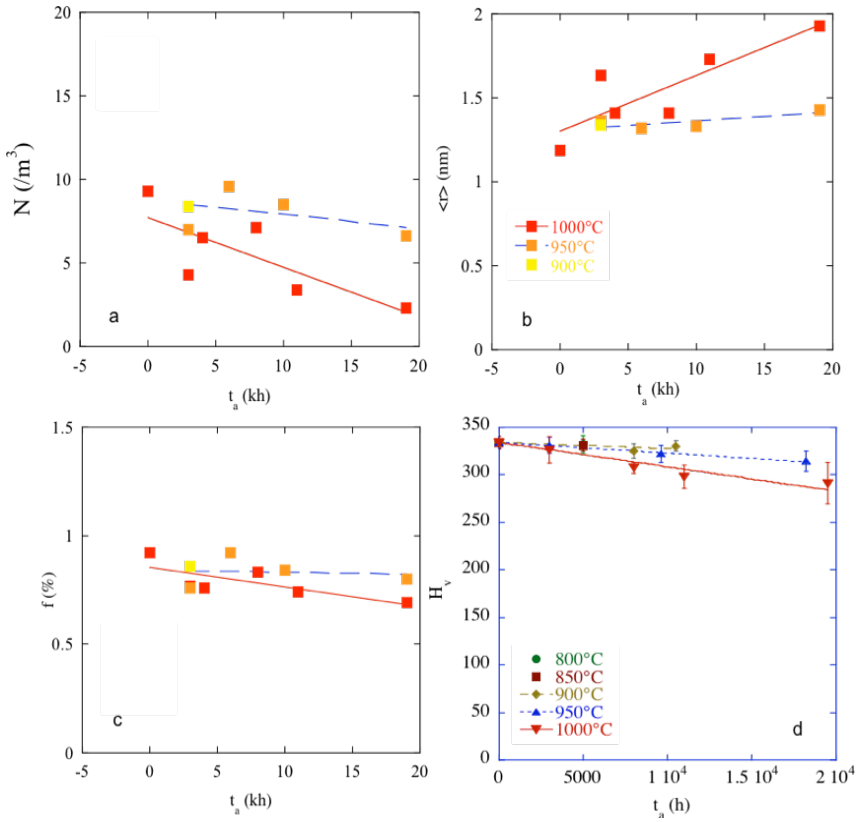

Figure 8. SANS measurements of a) N, b) <r> and C) f for LTTA at temperatures up to 1000°C and times in excess of 19 kh; d) corresponding microhardness changes.

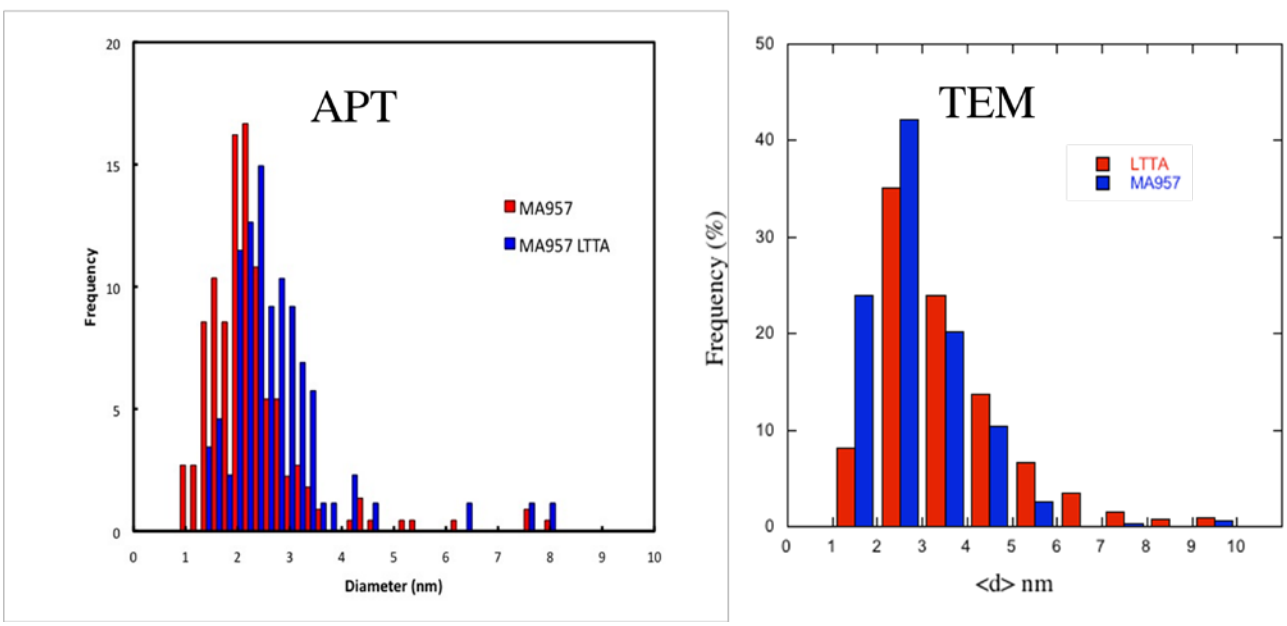

Figure 9. NF size distributions in as-extruded and LTTA MA957 measured by a) APT and b) TEM.

REFERENCES

1. G.R. Odette, M.J. Alinger, and B.D. Wirth, *Annual Review of Materials Research*, Vol. 38, (2008) 472.
2. G.R. Odette and D.T. Hoelzer, *JOM*, 62-9 (2010) 84.
3. G. R. Odette et al., *Trans. ANS,* 98 (2008) 1148.
4. G. R. Odette, P. Miao, D. J. Edwards, T. Yamamoto, R. J. Kurtz and H. Tanigawa, "Helium Transport, Fate and Management in Nanostructured Ferritic Alloys: In Situ Helium Implanter Studies," accepted for J Nuc Mater (2010).
5. Fisher JJ. 1978. Dispersion strengthened ferritic alloy for use in liquid-metal fast breeder reactors. *U.S. Patent No. 4,075,010.*
6. I.-S. Kim, J.D. Hunn, N. Hashimoto, D.L. Larson, P.J. Maziasz, K. Miyahara, and E.H. Lee, *J. of Nucl. Mater.*, 280 (2000) 264.
7. H.L. Hamilton, D.S. Gelles, R.J. Lobsinger, G.D. Johnson, W.F. Brown, M.M. Paxton, R.J. Puigh, C.R. Eiholzer, C. Martinez, and M. A. Blotter, "Fabrication Technological Development of the Oxide Dispersion Strengthened Alloy MA957 for Fast Reactor Applications", Technical Report PNL-13168, (1991).
8. P. Miao, G.R. Odette, T. Yamamoto, M. Alinger, D. Klingensmith, J. Nucl. Mater. 377 (2008) 59.
9. P. Miao, G.R. Odette, J. Gould, J. Bernath, R. Miller, M. Alinger, and C. Zanis, J. Nucl. Mater. 367-370 (2007) 1197.
10. J. Bernath, J. Gould, Report on Development of Candidate Joining Technology for MA957 Sheet, Edison Welding Institute, Columbus, OH, USA, March, 2005.
11. Glinka, C.J., Barker, J.G., Hammouda, B., Krueger, S., Moyer, J.J., and Orts, W.J., *J. Appl. Cryst.*, 31, 1998, 430.
12. M.J. Alinger, *On the formation and stability of nanometer scale precipitates in ferritic alloys during processing and high temperature service*, Ph.D Thesis, University of California, Santa Barbara, (2004).
13. M.J. Alinger, G.R. Odette, and D.T. Hoelzer, Acta Mater, 57 (2009) 392.
14. Mader, E., *Kinetics of irradiation embrittlement and post-irradiation annealing of nuclear reactor pressure vessel steels*, Ph.D. Thesis, University of California, Santa Barbara, (1995).
15. M. K. Miller, *Atom Probe Tomography: Analysis at the Atomic Level*, Kluwer Academic/Plenum Publishers, New York (2000).
16. K. Thompson, D. Lawrence, D.J. Larson, J.D. Olson, Kelly, T.F., and B. Gorman, Ultramicroscopy, 107 (2007) 131.
17. E. Oltman, R.M. Ulfig, and D.J. Larson, Microscopy and Microanalysis, 15 Supplement 2 (2009) 256-257.
18. D. Vaumousse, A.Cerezo, P.J. Warren, Ultramicroscopy 95 (2003) 215.
19. J.M. Hyde, C.A. English, in: G.E. Lucas, M. A. Kirk Jr, R.G. Elliman (Eds.), Proc. of the MRS 2000 Fall Meeting, Symp. R: *Microstructural Processes in Irradiated Materials* 650, Materials Research Society (2000/2001) R6.6.1.
20. R.P. Kolli and D.N. Seidman, *Microsc. Microanal.*, 13 (2007) 272.
21. C.A. Williams, E.A. Marquis, A. Cerezo, G.D.W. Smith, J. Nucl. Mater. 400 (2010) 37.
22. E.A. Marquis, Appl. Phys. Lett., 93 (2008) 181904
23. E.A. Marquis, F. Vurpillot, Microsc. Microanal. 14 (2008) 561.